• Original Paper •

Role of the Nocturnal Low-level Jet in the Formation of the Morning Precipitation Peak over the Dabie Mountains

Peiling FU[1,2], Kefeng ZHU[*1], Kun ZHAO[1], Bowen ZHOU[1], and Ming XUE[1,3]

[1]*Key Laboratory of Mesoscale Severe Weather/Ministry of Education and School of Atmospheric Sciences,*
Nanjing University, Nanjing 210093, *China*
[2]*Guangzhou Meteorological Observatory, Guangzhou* 511430, *China*
[3]*Center for Analysis and Prediction of Storms, University of Oklahoma, Norman Oklahoma* 73072, *USA*

ABSTRACT

The diurnal variation of precipitation over the Dabie Mountains (DBM) in eastern China during the 2013 mei-yu season is investigated with forecasts of a regional convection-permitting model. Simulated precipitation is verified against surface rain-gauge observations. The observed morning precipitation peak on the windward (relative to the prevailing synoptic-scale wind) side of the DBM is reproduced with good spatial and temporal accuracy. The interaction between the DBM and a nocturnal boundary layer low-level jet (BLJ) due to the inertial oscillation mechanism is shown to be responsible for this precipitation peak. The BLJ is aligned with the lower-level southwesterly synoptic-scale flow that carries abundant moisture. The BLJ core is established at around 0200 LST upwind of the mountains. It moves towards the DBM and reaches maximum intensity at about 70 km ahead of the mountains. When the BLJ impinges upon the windward side of the DBM in the early morning, mechanical lifting of moist air leads to condensation and subsequent precipitation.

Key words: nocturnal boundary layer, low-level jet, diurnal variation, precipitation, Dabie Mountains, mei-yu season

1. Introduction

The Yangtze–Huai River Basin (YHRB) is one of the major torrential rain centers in China (Zheng et al., 2016). The mei-yu season, typically starting around mid-June and lasting for one month or so, is one of the major rain periods in the YHRB. During the mei-yu season, a cold air mass from the north and warm moist air mass from the southern oceans associated with the summer monsoon converge in the YHRB, forming a roughly west–east rain band, thousands of kilometers long, along the quasi stationary mei-yu front (Ding, 1992). Persistent precipitation leads to extreme flooding, causing billions of dollars' worth of annual losses. Although progress has been made in the prediction of large-scale mei-yu front precipitation, local extreme rainfall, usually caused by meso-β and meso-γ convective systems are still hard to predict (Chen and Li, 1995; Li et al., 1997; Geng et al., 2009).

Previous studies on precipitation diurnal variations of the YHRB have focused more on large-scale circulations. In the YHRB, diurnal variations of precipitation have been shown to exhibit bimodal structures (Ding and Chan, 2005; He et al., 2016, 2017), with one peak in the early morning and the other peak in the late afternoon (Yu et al., 2007; Chen et al., 2009; Yuan et al., 2010, 2012; Luo et al., 2013a). The afternoon peak is clearly associated with convective precipitation due to daytime solar heating (Xu and Zipser, 2011), while the formation mechanism of the early morning peak is not as well understood. There are three major views. The first attributes the cause to the eastward propagation of convective systems, originally forming over the Tibetan Plateau in the afternoon (Wang et al., 2005; Bao et al., 2011; Xu and Zipser, 2011) and then propagating eastward. When reaching the YHRB, the organized mesoscale convective systems (MCSs) usually intensify in the evening and result in the morning peak precipitation in that region. But during the mei-yu season, especially during the post-mei-yu period, the propagating MCSs retreat to the west of the YHRB, and are no longer responsible for the morning rainfall (Wang et al., 2005; Bao et al., 2011). The second mechanism associates the morning peak with large-scale thermally induced circulations between the mountains in central China and the eastern plains, known as the mountain-plains solenoid (MPS) (Sun and Zhang, 2012). During the mei-yu season, convective cells form in the lee-

---

* Corresponding author: Kefeng ZHU
  Email: kefeng@nju.edu.cn

side of the Wushan Mountains (~114°E) in the daytime and then move eastward along the mei-yu front. When reaching the YHRB at night, the upward branch of the MPS circulation helps convective cells evolve into strong MCSs that reach maximum intensity in the early morning. For this mechanism, the synoptic-scale southwesterly low-level jet (SLJ) at 850 hPa plays an important role in transporting moisture from the Bay of Bengal, alongside that from land surface evaporation (Yamada et al., 2007), into the YHRB. As reported in Chen et al. (2010) and Yuan et al. (2013), an anomalous (i.e., accelerated) low-level southwesterly flow and an anomalous northeasterly (i.e., decelerated southwesterly) flow converge over the YHRB at 0800 LST, resulting in a favorable zone of storm formation and intensification. The third mechanism suggests that locally initiated MCSs tend to form in the late afternoon and early evening in the YHRB. The time lag between the initiation and mature phase of the MCSs leads to maximum rainfall during late night and early morning (Wallace, 1975; Dai et al., 1999; Nesbitt and Zipser, 2003).

The Dabie Mountains (DBM), with the highest peak of 1774 m and several others topping 1500 m, is a major mesoscale terrain in the YHRB and has important effects on storm propagation and rainfall distributions. Long-term averages from various observations show that the DBM is one of the local precipitation centers in the YHRB, with rainfall mainly located at the main peak area and its upwind region (Luo et al., 2013b; Zheng et al., 2016). Along the synoptic mei-yu front, the rain center at the DBM appears as an embedded local hotspot. In this study, we focus on explaining the mechanism of the morning precipitation peak during a mei-yu period over the DBM and its upwind range. Complementary to past studies, which mostly analyzed the synoptic-scale forcing on the morning rainfall peak, this study uncovers a new mechanism responsible for the nighttime upslope flow on the windward (relative to the prevailing synoptic-scale wind direction) side of the DBM. This mechanism appears to be the most pronounced factor causing the early morning rainfall peak over the DBM.

The rest of this paper is organized as follows: In section 2, the data used, including forecasts from the Nanjing University 4-km real-time forecast system and rain gauge observations, are introduced. The forecasting results and the rainfall peak mechanism are discussed in sections 3 and 4, respectively. In section 5, a mei-yu front case is presented to further illustrate the contribution of a nocturnal boundary layer low-level jet (BLJ) and the DBM. A summary and discussion are provided in section 6.

2.   Model description and observational data

The forecast data are from the 4-km Nanjing University real-time forecast system (Zhu et al., 2018), which uses the Weather Research and Forecasting (WRF) model (Skamarock et al., 2005) (hereafter referred to as NJU_WRF). NJU_WRF runs to 48 hours twice a day from 1 June through 31 August every year since 2013. Precipitation evaluations

(e.g., Zhu et al., 2018) have shown that NJU_WRF performs better than both regional and global operational models, such as ECMWF, NCEP GFS, JMA and CMA global forecasts, over mainland China, especially for heavy rain forecasts.

NJU_WRF has a 4 km horizontal grid spacing and 51 vertical levels extending to 50 hPa. Such a grid spacing is considered convection permitting and is able to resolve midlatitude MCSs (Weisman et al., 1997; Mass et al., 2002). Initial and lateral boundary conditions are obtained from the NCEP real-time GFS (0.5°). The land surface processes are represented by the Pleim–Xiu scheme (Pleim, 2006). Other key parameterizations include the Morrison double-moment microphysics scheme (Morrison et al., 2005), the Pleim–Xiu planetary boundary layer scheme (Pleim, 2007), and the CAM radiation scheme (Collins et al., 2004). This set of parameterizations was evaluated and considered appropriate for use over China, especially for heavy rainfall (Zhu and Xue, 2016).

The simulation domain of NJU_WRF covers the whole of mainland China (see small panel in Fig. 1). In this study, only part of the model domain covering the YHRB is used for the analyses (see Fig. 1). To investigate precipitation over the DBM and its upwind sides, time series of mean precipitation are calculated within the red rectangle in Fig. 1. The 12–36-h forecasts initiated at 0000 UTC are used for the statistics.

The precipitation forecasts are validated against a dense network of surface rain gauges (more than 30 000 sites) in China. In some provinces near the coast, the mean distance between sites is about 7 km. For this study, hourly rain-gauge data from 1607 surface stations around the DBM were collected and quality controlled. Additionally, daily soundings at a nearby sounding site [station number 57494 at (30.62°N, 114.13°E), marked by the cross in Fig. 1] are used to validate simulated wind profiles. This sounding site is chosen also because it is on the upwind side of the mountains with respect to the synoptic southwesterlies during the mei-yu season.

3.   Description of mean precipitation patterns

Figure 2 presents the mean 24-h accumulated rainfall for both observations and NJU_WRF forecasts averaged over the 2013 mei-yu period from 23 June through 10 July. The observations in Fig. 2a show a clear heavy-rain center over the DBM with a long tail extending southwest in the upwind direction and a short tail to the east of the mountains. The precipitation in the NJU_WRF forecasts in Fig. 2b displays similar overall patterns. The forecasts successfully capture the rainfall center over the DBM but underestimate precipitation on both sides. In this study, we focus on precipitation over the DBM and its upwind region.

Time series of observed and simulated hourly rainfall $\langle \overline{R} \rangle$ over the DBM are presented in Fig. 3, where angle brackets indicate the spatial average within the red rectangle in the analysis domain shown in Fig. 1 and an overbar represents the temporal average over the 18 days of the 2013 mei-yu season. A bimodal pattern stands out in the observations. The
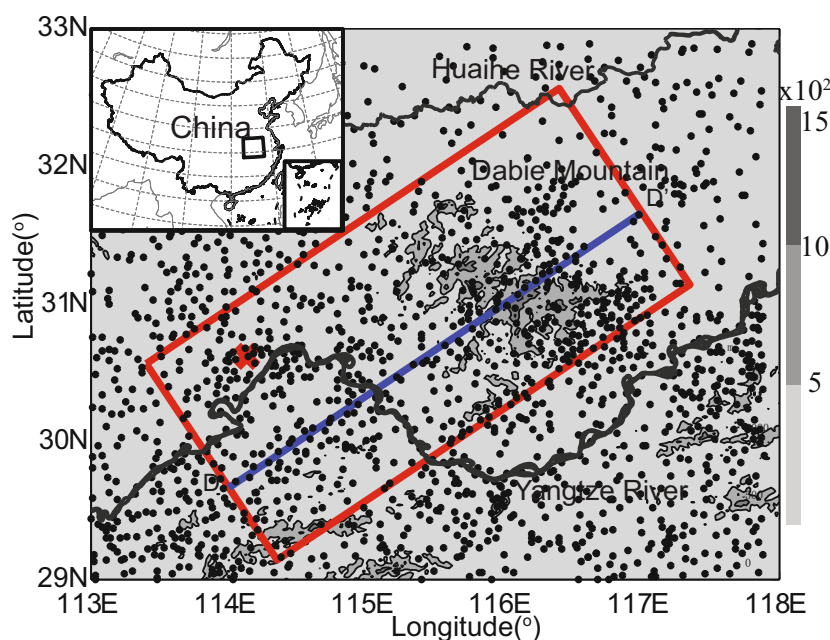
Fig. 1. The analysis domain of the DBM. Terrain height is shown in gray shaded contours at 500-m intervals. The red rectangle represents the analysis region of Fig. 3. The rectangle is aligned with the prevalent 850-hPa geostrophic wind direction. The blue line indicates the location of the vertical cross section presented in Fig. 11. The location of an upwind sounding site (57494) is marked by a red cross (used in Fig. 6). The top-left inset marks the location of the analysis domain with respect to the entire forecast model domain. The black dots are the locations of rain gauge stations.

averaged precipitation $\langle \overline{R} \rangle$ increases from 0400 LST onwards, and peaks at 0800 LST. Afterwards, $\langle \overline{R} \rangle$ decreases before increasing again slightly around noon, resulting in a smaller local peak at 1300 LST. In the afternoon, $\langle \overline{R} \rangle$ decreases continuously until it reaches its minimum at 2000 LST. The forecasts reproduce the observed early morning and noon peaks with similar magnitudes, but with an hour's delay. The simulated diurnal minimum precipitation is found around 1900 LST, which is an hour earlier than in the observations. The correlation coefficient between the observation and forecast time series is as high as 0.83.

The spatial distributions of hourly accumulated precipitation from evening to early morning reveal the details of the formation of the morning rainfall peak (Fig. 4). Right after sunset at 2000 LST (Fig. 4a), precipitation activities appear least active, corresponding to the observed diurnal minimum in Fig. 3. Some scattered rainfall areas are found over the west and the southeast plains, away from the DBM. Only a few precipitation spots are found at the foot of the DBM. Later, at 0200 LST, the precipitation cluster propagates to the mountains, and rainfall in the upwind region intensifies (Fig. 4c). From 0500 (Fig. 4e) to 0800 LST (Fig. 4g), an obvious increase in rainfall occurs along the windward (relative to the prevailing synoptic-scale wind) side of the DBM, and a rain band forms that is oriented approximately southwest to northeast. The intense rainfall around the DBM corresponds to the morning precipitation maximum observed in Fig. 3.

The WRF forecasts capture the major spatial features of

the nighttime to morning rainfall (right-hand panel of Fig. 4), including the propagation at late night (from 2000 to 0200 LST) and rainfall intensification in the morning (from 0500 to 0900 LST). Note that the predicted rainfall peak is delayed by about an hour compared to that of the observations (see Fig. 3). To account for this delay, the 0900 LST forecast is presented instead of using the same time as the observation. Overall, the 4-km NJU_WRF forecasts successfully reproduce the observed morning rainfall peak and capture the 24-h diurnal precipitation pattern (Fig. 3). In the following section, we use NJU_WRF forecasts to investigate the mechanism of rainfall from early morning to a few hours after sunrise.

4. Low-level jet and the morning rainfall peak

During the mei-yu season, the lower half of the troposphere over East China is dominated by an anticyclonic circulation associated with the western Pacific synoptic high. The prevailing winds in the YHRB at 950 hPa low-levels are nearly southwesterly (Fig. 5). A prevalent low-level jet is found in the southwest of the DBM. It is part of the northernmost extent of the southwesterly monsoon flow. The DBM are located along the path of the southwesterly flow, which has an abundant supply of moisture and is a favorable location for rainfall.

Figure 6 presents the vertical profiles of wind speed at the windward side (see cross sign in Fig. 1) at 1200 and 0000 UTC (2000 and 0800 LST). Uncertainties associated with the
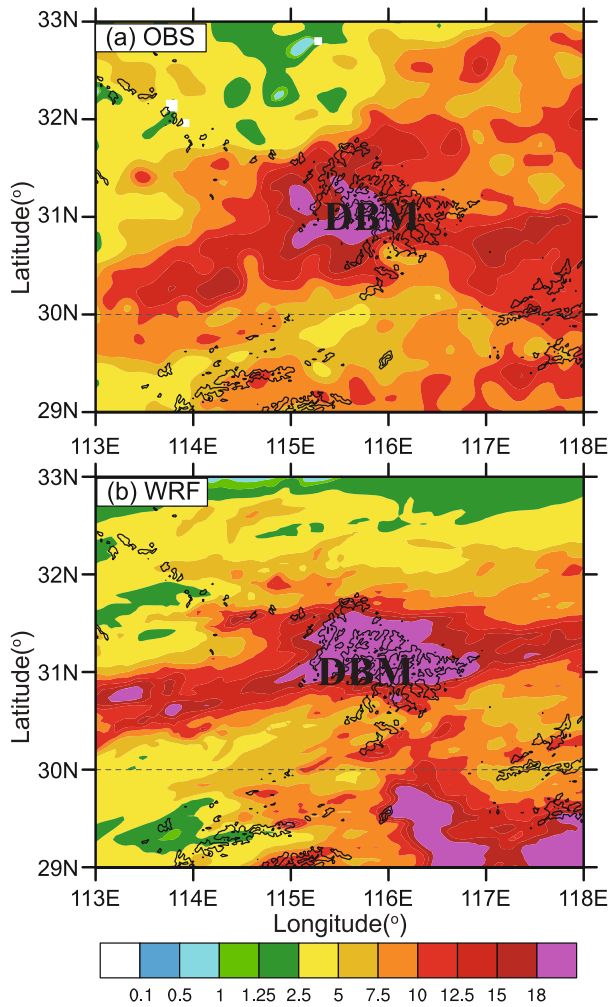
Fig. 2. (a) Mean observed 24-h accumulated rainfall (units: mm) during the 2013 mei-yu period from 23 June to 7 July, and (b) mean 24-h accumulated rainfall from WRF forecasts over the same period. Terrain height is shown in black contours with 500 m interval.
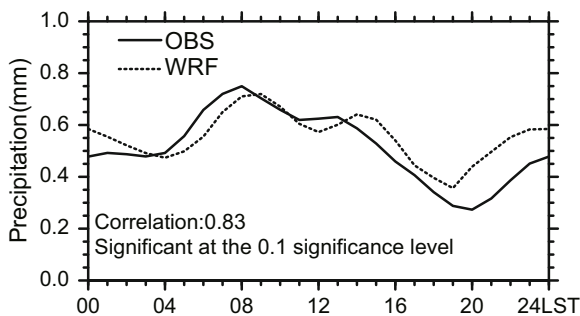
Fig. 3. Times series of observed (OBS) and simulated (WRF) temporally and spatially averaged hourly rainfall over the DBM. The spatial average is calculated over the area represented by the red rectangle in Fig. 1. The temporal average is calculated over the entire 2013 mei-yu season.

observation and forecast almost overlay each other, which means that there is no significant difference between the two.

From evening to early morning, both observations and WRF forecasts exhibit intensification of wind speeds in the lower half of the troposphere, with the maximum wind speed located between 950 and 925 hPa. However, for both times, the forecast wind speeds are higher than the observations at lower elevations and the forecast height of maximum wind speed is closer to the surface. Note that the observed soundings are only available at specific levels. The differences between observations and WRF forecasts are partly attributable to inadequate observation levels at lower elevations. The potential temperature (θ) profiles from the observations and the forecasts are also presented in Fig. 6. The forecasts reach overall agreement with the observations, except close to the surface. At 0800 LST, the WRF-forecasted θ has a cold bias between 1000 and 950 hPa of up to 2 K. This indicates a shallower nighttime stable boundary layer in the forecasts. This might correspondingly lower the peak of the forecasted boundary layer low-level jet, as shown in Fig. 6b.

The SLJ exists between 900 and 600 hPa, with maximum winds usually located between 850 and 700 hPa (Chen et al., 1994, 1997; Du et al., 2012). Being a synoptic-scale flow phenomenon, the SLJ does not exhibit apparent diurnal variations. The BLJ, on the other hand, is associated with significant diurnal variations (Du et al., 2012). Over land, in addition to the thermally induced MPS mechanism mentioned in the introduction, the Blackadar mechanism should be taken into consideration (Blackadar, 1957; Du et al., 2015) for the BLJ's formation. During daytime, a near balance is achieved among the pressure gradient force, the Coriolis force, and the frictional force. With surface cooling at night, the near-ground static stability increases, which acts to suppress turbulent mixing. As a result, the middle and upper portions of the boundary layer become decoupled from the surface layer. The force balance in the layer residing between roughly 500 to 1500 m above ground level is disrupted, because the frictional force is effectively turned off. This force imbalance causes an inertial oscillation of the winds, which leads to super-geostrophic winds and a nocturnal low-level wind maximum in the overnight hours (Blackadar, 1957; Van De Wiel et al., 2010). Given the formation mechanism of the BLJ, its nighttime peak magnitude is set by the background geostrophic flow and the daytime time frictional forcing. As shown by the color shading in Fig. 5, the diurnal-averaged wind speeds, which are representative of the background flow, varies spatially around the DBM. Wind speeds southwest of the DBM (i.e., the windward side) are generally higher than those on the northeast leeward side. With similar daytime heating, which is mostly dictated by solar radiation, spatial variations of the BLJ strength in the DBM region are expected as a result of the differences in the background flow (This is evidenced later in Fig. 9).

Vertical profiles of the wind speeds upwind of the DBM are presented in Fig. 7 at 3-h intervals to demonstrate the diurnal cycle of winds and the nighttime formation of the BLJ. The wind speeds are averaged over the black box in Fig. 5. The nighttime acceleration of winds from 1700 LST onwards is observed in the boundary layer up to around 850 hPa. Wind
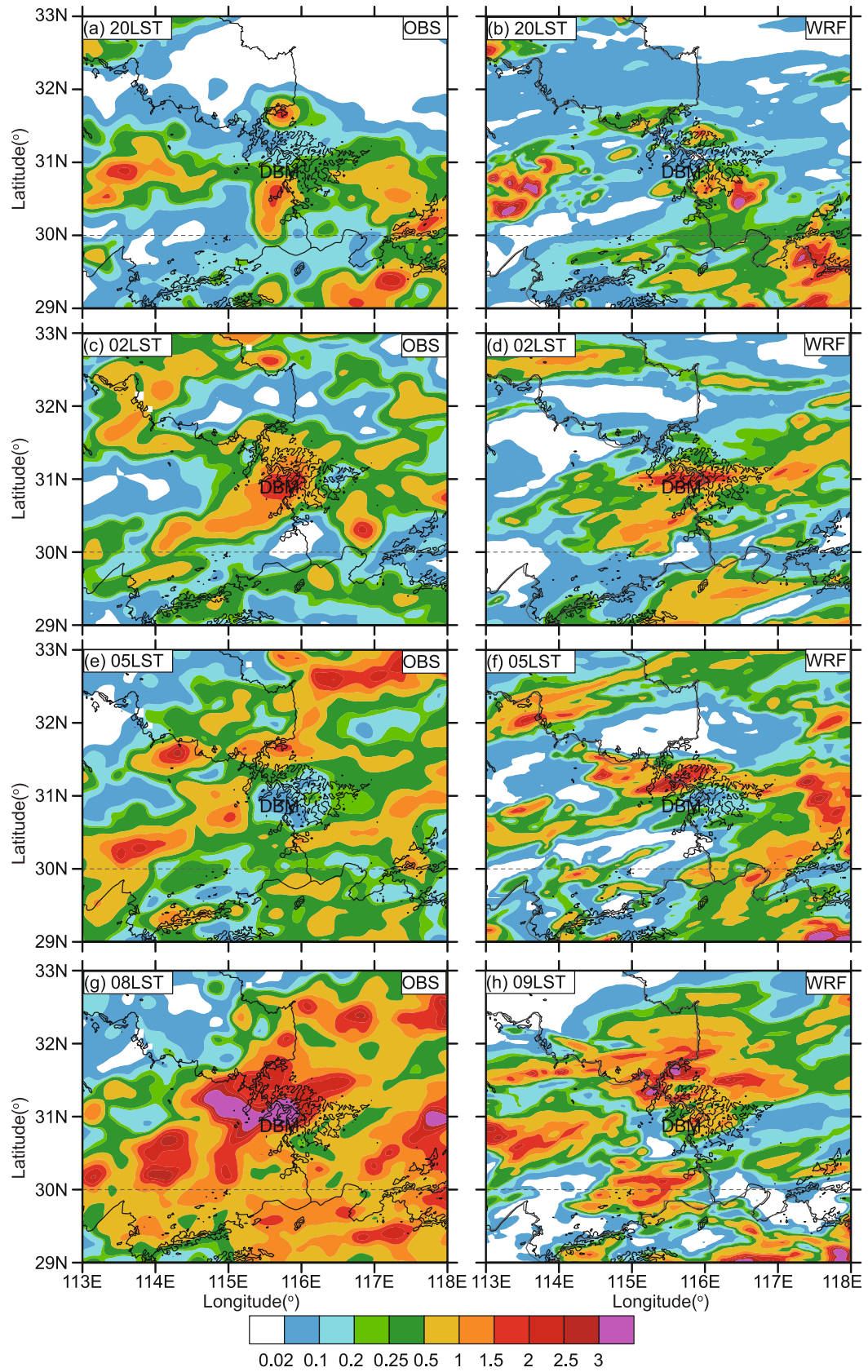
Fig. 4. Shaded contours of time-averaged hourly accumulated rainfall (units: mm) from surface rain gauge measurements at 2000, 0200, 0500 and 0800 LST. The left-hand panels are from observations and the right from the NJU_WRF forecasts. Terrain height is superimposed as black contours at 500-m intervals. The rain gauge observations are remapped onto the WRF grid using bilinear interpolation. Terrain height is shown in black contours with 500 m interval.
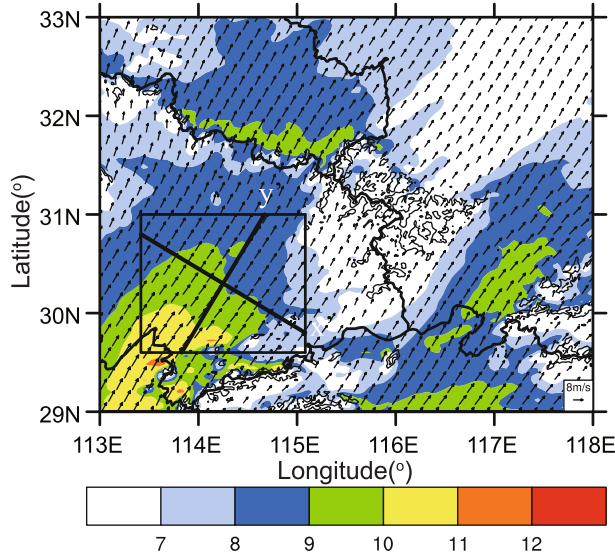
Fig. 5. Time-averaged, WRF-simulated wind vectors at 950 hPa. Shading represents the wind speeds at 950 hPa. The black rectangle marks the area used in the momentum budget analysis in Fig. 8. Terrain height is shown in black contours with 500 m interval.

speeds peak at 0500 LST between 950 and 900 hPa, reaching over 12 m s^{-1}. From then on, winds decelerate as friction associated with the daytime boundary layer increases.

To investigate the forces responsible for the formation of the BLJ, time series of the forcings in the momentum budget are presented in Fig. 8.

$$\underbrace{\frac{\partial v}{\partial t}}_{\text{I}} = \underbrace{-\left(u\frac{\partial v}{\partial x'}+v\frac{\partial u}{\partial y'}\right)}_{\text{II}}+\underbrace{f(U_g-u)}_{\text{III}}+\underbrace{F}_{\text{IV}} \qquad (1)$$

The axes are rotated such that the new y'-axis is aligned with the BLJ direction as shown in Fig. 5, where u and v are the wind components in the x' and y' directions, and U_g is the corresponding geostrophic wind. The four terms of Eq. (1) represent the tendency (Term I), horizontal advection (Term II), Coriolis force acting on ageostrophic wind (Term III), and frictional force (Term IV), respectively. The frictional force is computed as a residual term following Du et al. (2014). The budget terms are spatially averaged within a box around the sounding site in Fig. 5 to obtain representative conditions of the upstream flow. Time series of the wind component
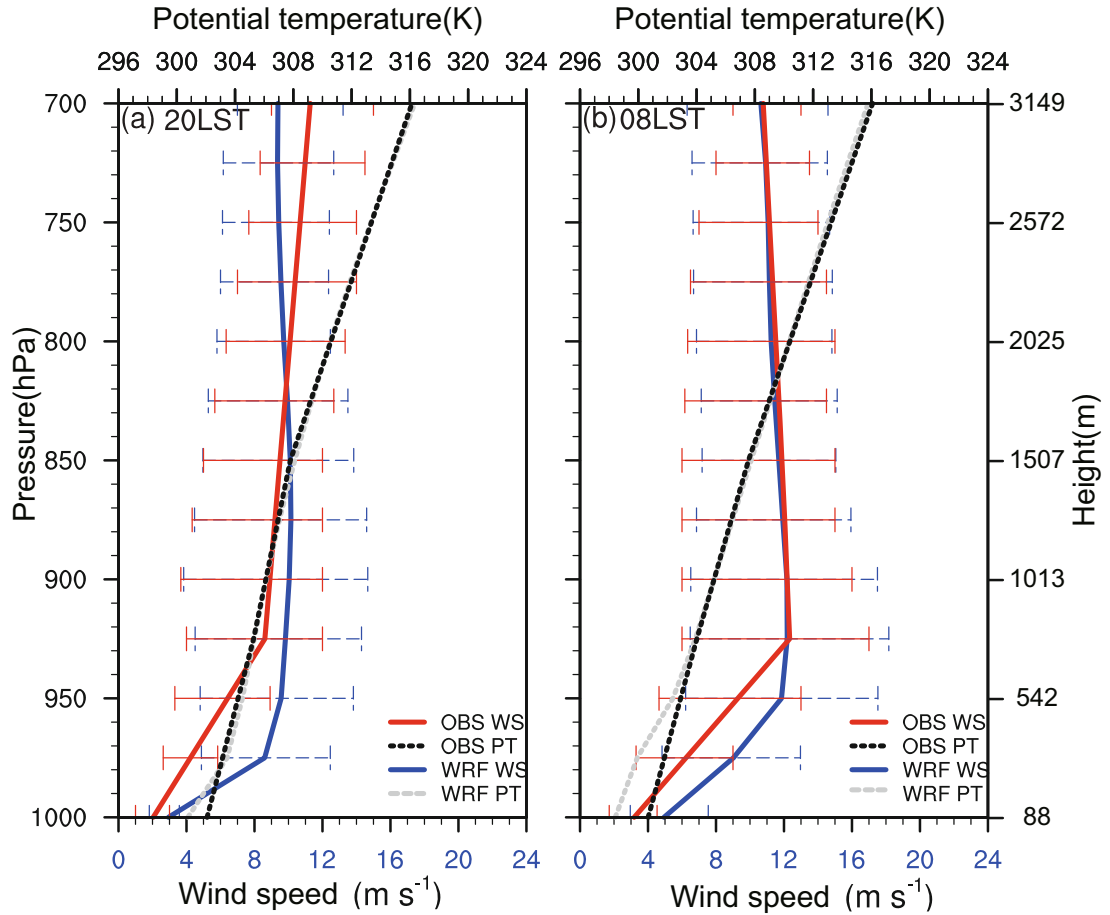
Fig. 6. Time-averaged vertical wind and potential temperature profiles at the sounding site indicated in Fig. 1 at (a) 1200 UTC (2000 LST) and (b) 0000 UTC (0800 LST), with the 25th/75th percentiles of wind data represented by horizontal error bars. The NJU_WRF results are spatially averaged over a 1° × 1° box centered on the sounding site. The temporal averaging was calculated over the entire 2013 mei-yu season, using 12- and 24-h forecasts from 1200 UTC, respectively, corresponding to the times of twice-daily soundings. The solid and dashed lines represent the observed and NJU_WRF-forecast soundings, respectively.
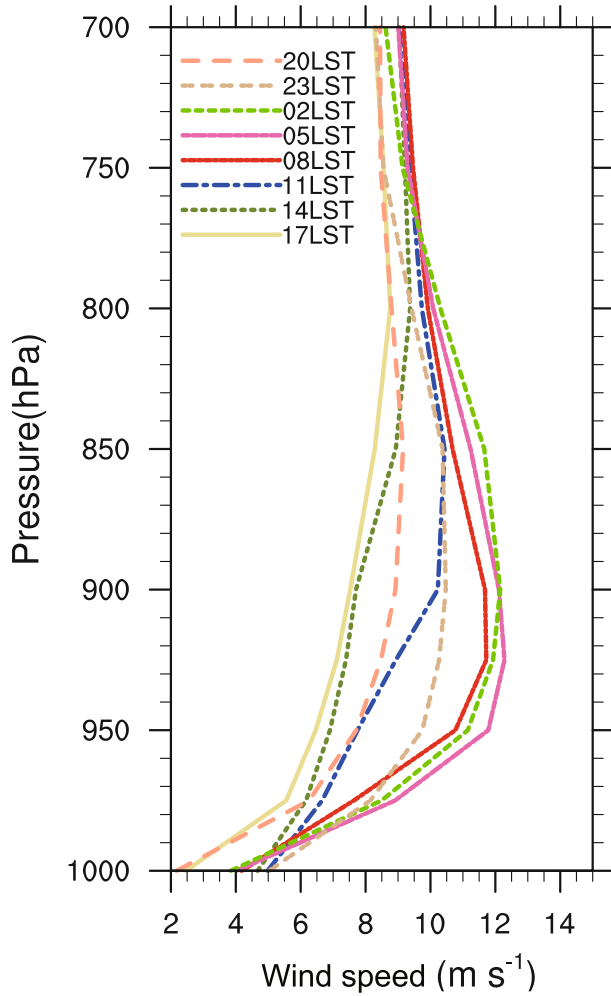
Fig. 7. Vertical profiles of wind speeds at 3-h intervals averaged over the area represented by the black box in Fig. 5.
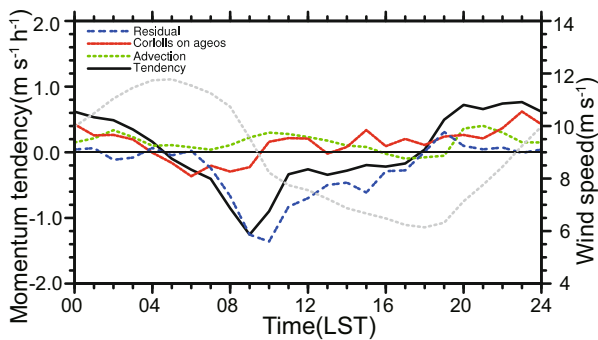
Fig. 8. Diurnal variations of individual terms in the horizontal momentum equation at the 950-hPa level averaged over the upwind region (inside the black rectangle in Fig. 5) of the DBM. The momentum budget in the y' direction is calculated. Term I: Tendency; Term II: Advection; Term III: Coriolis on ageostrophic; Term IV: Residual. The gray dashed line is the average wind speed inside the black rectangle in Fig. 5.

along the y'-axis averaged over the same area are also presented in Fig. 8. Given the latitudes of the DBM at 31°N ($f = 0.75 \times 10^{-4}$ s^{-1}), the period of the inertial oscillations

is close to 24 hours ($2\pi/f = 23.3$ h). The wind component exhibits strong diurnal variation, with low speeds during the day and high speeds at night. The maximum and minimum wind speeds occur in the early morning at around 0500 LST and late afternoon at 1800 LST, respectively. The tendency term, which is responsible for the changes in wind speed, exhibits similar patterns, with negative (positive) values during daytime (nighttime). Among the three forcings on the right-hand side of Eq. (1), the Coriolis force acting on the ageostrophic wind dominates the tendency term at nighttime between around 2100 to 0600 LST when the friction term is almost zero. During that time, the contribution of the advection term is also very small. At sunrise, shortly after 0600 LST, the frictional force suddenly increases (becomes more negative) due to the onset of daytime boundary layer convection. It reaches its maximum at 1000 LST and then decreases steadily for the rest of the daytime. The frictional force is largely responsible for the changes in the overall tendency for the daytime. Overall, the frictional force dominates the momentum tendency during the daytime, while the Coriolis force acting on the ageostrophic wind plays an important role for nighttime.

A signature of the nocturnal BLJ is the inertial oscillation (i.e., clockwise turning in the Northern Hemisphere) of the low-level winds with time. This is presented in Fig. 9 where the perturbation wind vectors at the 950-hPa elevation is plotted at every 3 h during the course of the day. The perturbation winds from the NJU_WRF forecasts are computed by subtracting the daily mean values from the winds at every grid point. To help visualize veering of the winds, thick open arrows are drawn in each subfigure to indicate the dominant direction of the winds southwest of the DBM. The magnitudes of the upstream perturbation wind vectors, spatially averaged winds over the black box in Fig. 5, are presented in the hodograph in the middle panel of Fig. 9. The clockwise turning of the upstream winds unaffected by the DBM over a period of approximately 24 h is well simulated by the 4-km NJU_WRF.

Notably, in Fig. 9, the perturbation winds are pointing towards the southwest direction against the dominant background southwesterly flow during the daytime (see Figs. 9e–h). In contrast, in the evening, the perturbation wind vectors gradually turn to align with the synoptic flow, and enhance the supply of moisture towards the DBM (see Figs. 10a–c), creating favorable conditions for moist convection. The formation and development of the jet at nighttime is visualized by the color contours indicating the magnitudes of the perturbation winds. At 0200 LST in Fig. 9b, some fast-moving strips of air, indicated by the orange colors, start to form in the southwest corner of the model domain, about 200 km away from the DBM in the upwind direction. (Note that the spatial inhomogeneity of the jet speed is a consequence of the variations of the background flow as illustrated in Fig. 5. Veering of the wind vectors occurs unanimously within the model domain). Correspondingly, the strength of water vapor flux in the windward region of the DBM is greatly enhanced (see Fig. 10b). At 0500 LST (Fig. 9c), the core of the jet has ad-
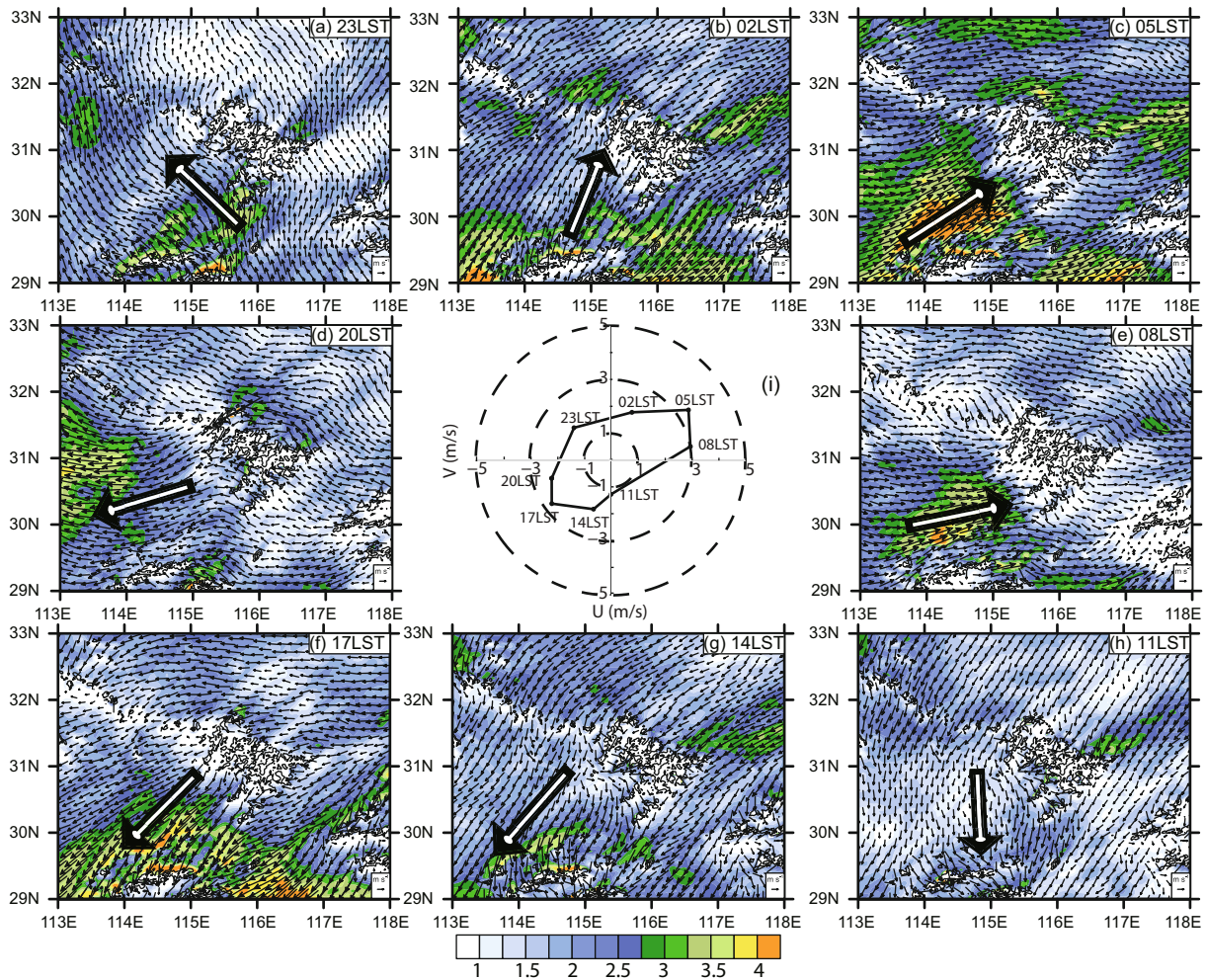
Fig. 9. (a–h) Mean simulated 950-hPa perturbation wind speed (shaded; units: m s^{-1}) and wind vector every 3 h. Perturbations at each grid point are computed by subtracting the daily-mean values at that grid point. (i) Hodograph of 950-hPa perturbation winds spatially averaged over a $1° \times 1°$ box centered at a sounding site indicated in Fig. 1, showing clear clockwise rotation. The temporal averaging is calculated over the entire 2013 mei-yu season. The thick open arrow in each panel indicates the general direction of perturbation wind vectors upwind of the DBM. Terrain height is shown in black contours with 500 m interval.

vanced much closer to the mountains, covering a wide area of the upwind region. Meanwhile, the strength of water vapor flux reaches its maximum (see Fig. 10c). The intensification of water vapor transport results in intense precipitation on the windward side of the DBM from 0500 LST to 0800 LST (note that rainfall may need some time to form after convective initiation). At 0800 LST (Fig. 9d), while the location and the spatial extent of the jet remain similar to the previous time, its strength is much weakened due to the onset of daytime boundary layer convection. Correspondingly, the intensity of water vapor flux begins to weaken (shown in Fig. 10d). Around noon (Fig. 9e), the jet completely disappears, and perturbation winds veer to weak northerly flows.

As shown in Fig. 9, the BLJ forms initially around 0200 LST, reaches its maximum intensity and widest spatial coverage at 0500 LST, and weakens at 0800 LST. To further investigate the vertical extent of the BLJ, perturbation winds projected onto the vertical cross sections are presented in Fig. 11. The direction of the vertical slice is along the y'-axis

in Fig. 5. At 0200 LST (Fig. 11a), a BLJ forms at the left-hand end of the vertical cross section on top of a weaker and much wider SLJ extending to 2 km above ground level. Wind speeds are enhanced between 250 m and 1 km. At 0500 LST, the BLJ strengthens significantly. The "nose" or the maximum wind speed of the jet is clearly visible at about 500 m above ground level (~950 hPa) between 115°E and 116°E, reaching the foothills of the DBM. After sunrise (Fig. 11c), the horizontal and vertical extents of the BLJ remain similar to the previous time, while the jet is weakened.

The changes of upstream winds with the formation and development of the BLJ offer a plausible explanation to the morning rainfall peak on the upwind side of the DBM. As the flow accelerates and impinges upon the mountain range, it is forced to reorient into an apparent updraft in the lower troposphere (Figs. 11b and c). Accompanied by the abundant low-level moisture of the background synoptic flow, the upward motions would lead to condensation and subsequent precipitation. The time lag between the maximum BLJ strength at
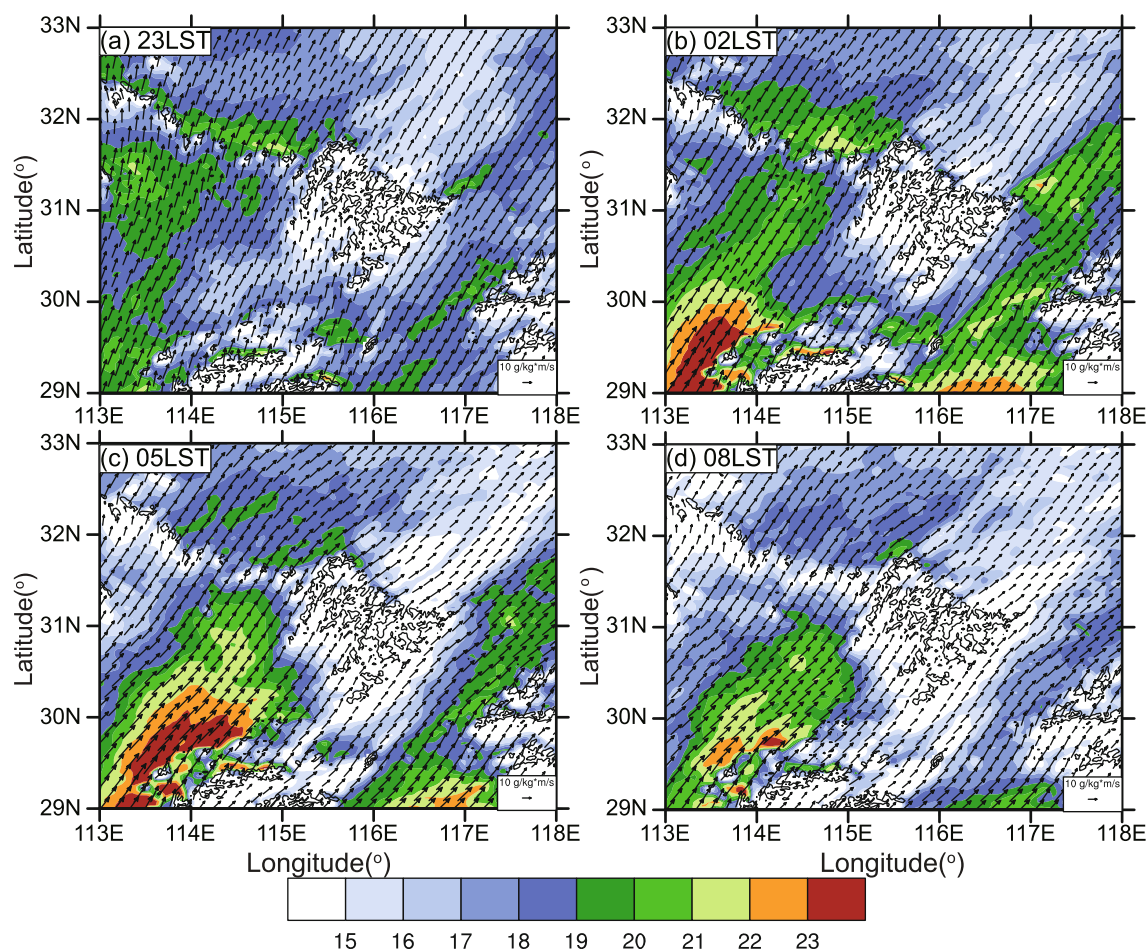
Fig. 10. Mean simulated 950-hPa vapor flux [shaded; units: g hPa^{-1} (cm s)$^{-1}$] and wind vector during the night: (a) 2300 LST; (b) 0200 LST; (c) 0500 LST; (d) 0800 LST. Terrain height is shown in black contours with 500 m interval.

0500 LST and the rainfall peak at 0800 LST (Fig. 3) is mainly due to the time needed for the development of moist convection.

While the results presented above point to a linkage between the nighttime BLJ (specifically, its associated moisture transport and its dynamic effects in enhancing the upslope flow) and the morning precipitation peak over the DBM, we are yet to establish a formal causal relationship between the BLJ and the morning rainfall. In the next section, we attempt to shed more light on this relationship by reporting the results of a sensitivity experiment conducted based on a typical case. Nevertheless, the conclusions drawn from the case study are still far from complete. More work will be needed before it is possible to claim that the BLJ is responsible for morning rainfall over the DBM. One important factor that should be considered in future work is the role of the mei-yu front, including its location and orientation with respect to the DBM, which sets the synoptic environment that affects the BLJ and the large-scale rainfall patterns.

5.   A mei-yu front case study

A typical mei-yu front case is selected to further illustrate the contribution of the BLJ and the mountain topography to
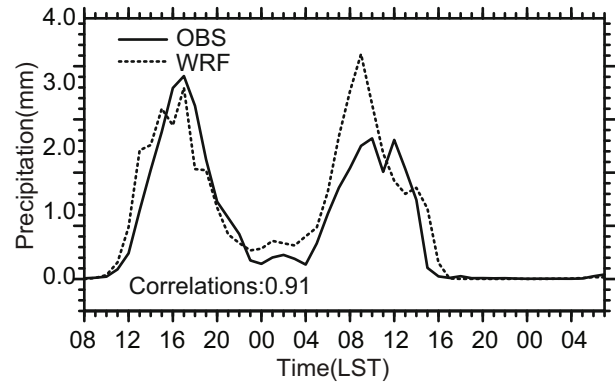
nighttime precipitation over the DBM. Figure 12 presents the diurnal precipitation time series of the forecast and the rain-gauge observations for the selected case on 24 June 2013. Similar to the time-averaged precipitation statistics (see Fig. 3) over the mei-yu period, a bimodal pattern is clear in both the forecast and observation, with one peak in the afternoon (1700 LST) and another in the morning between 0900 and 1000 LST. Here, the result from the real-time forecast is used as the control experiment.

Two additional experiments are conducted. The first experiment, NoSHF, is setup to investigate the impact of BLJ on precipitation, in which the surface heat flux is set to zero. Without the diurnal surface heat flux forcing, turbulent mixing processes in the boundary layer are driven solely by the geostrophic winds, day and night. Without vigorous turbulent mixing to offset the geostrophic balance during the daytime, the nighttime acceleration of the wind due to stability-limited turbulence is also absent. Correspondingly, no rapid intensification of low-level wind is observed in the boundary layer. By comparing the results of NoSHF with the control simulation, the contribution of the BLJ can be identified. The purpose of the other experiment, NoDBM, is to examine the contribution of the mountain topography. In this experiment, we set the terrain height of the DBM to 1/10 of their original height.
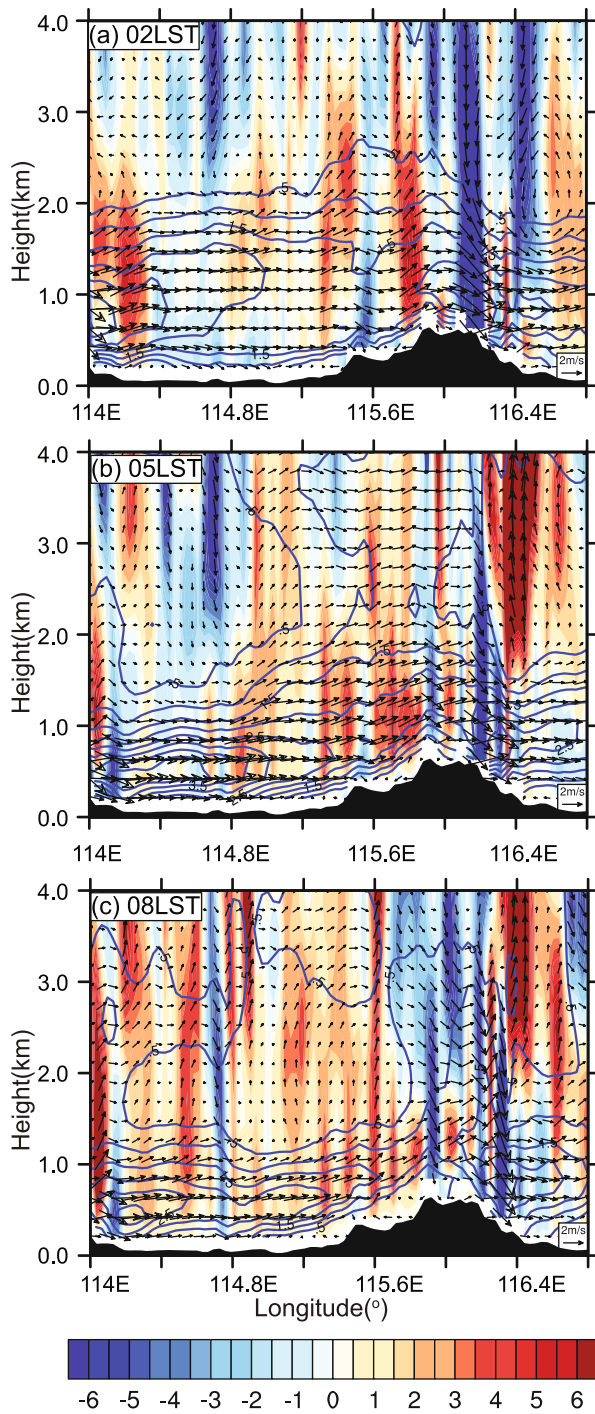
Fig. 11. Contours of time-averaged simulated vertical speed (shaded; units: 0.01 m s^{-1}) and perturbation (from the daily mean) wind speed (contours; units: m s^{-1}), and perturbation wind vectors at (a) 0200, (b) 0500 and (c) 0800, in a vertical cross section along the blue line in Fig. 1. The vertical wind speed is amplified by 100 times for the vector plotting to improve visualization. The temporal averaging is calculated over the entire 2013 mei-yu season. The black shaded represents terrain height.

The mean height of the DBM after adjustment is about 150 m, which is close to the height of the surrounding plain.


Fig. 12. Observed and forecast hourly mean precipitation rainfall over the DBM for a forecast start from 0000 UTC 24 June 2013. The spatial averaging is calculated over the area represented by the red rectangle in Fig. 1.

Figure 13 presents the results of three experiments. For the control experiment, at 0400 LST, convection (as indicated by red contours of higher than 35 dBZ reflectivity) forms in the convergence line mainly induced by the outflow of the mei-yu front and the northward water vapor flux (Fig. 13a). The intensification of convection between 0400 LST and 0800 LST is most likely attributable to the intensification of the northward water vapor flux (see Fig. 13b), since the northerly flow associated with the mei-yu front is still far away. Without diurnal oscillation of winds in the boundary layer, there is no continuous intensification of wind speed overnight. As we can see from experiment NoSHF, the strength of the BLJ is greatly reduced at 0800 LST and 0900 LST (see Figs. 13e and f). Also, the wind direction does not turn as the influx of water vapor approaches the DBM. The intensification of convection in the NoSHF experiment is likely associated with the southward moving mei-yu front. However, this does not mean the intensification of the BLJ has no impact on precipitation intensification along the convergence line. We believe that both the northerly (mei-yu front) and southerly flows (associated with the BLJ) contribute to intense precipitation in this region and the contribution from the two parts may be different depending on the strength of the BLJ.

From 0800 to 0900 LST, the transport of water vapor is reduced in the control experiment. The intensification of precipitation for that time period is due to orographic lifting by the DBM. Without the DBM, the strength of convection is clearly reduced (see Figs. 13h and i). The other impact of the DBM is from the barrier effect. Without the DBM, water vapor does not accumulate on the windward side. This can be seen more clearly in the vertical cross sections in Fig. 14. From 0700 to 0800 LST, in the control experiment, the strength of water vapor flux is greatly enhanced when approaching the DBM (Figs. 14a and b). Convection is enhanced when climbing up the DBM. When topography is essentially removed, the strength of water vapor flux does not intensify from 0700 to 0800 LST. Without the terrain barrier effect, at 0800 LST, the strength of water vapor flux of the
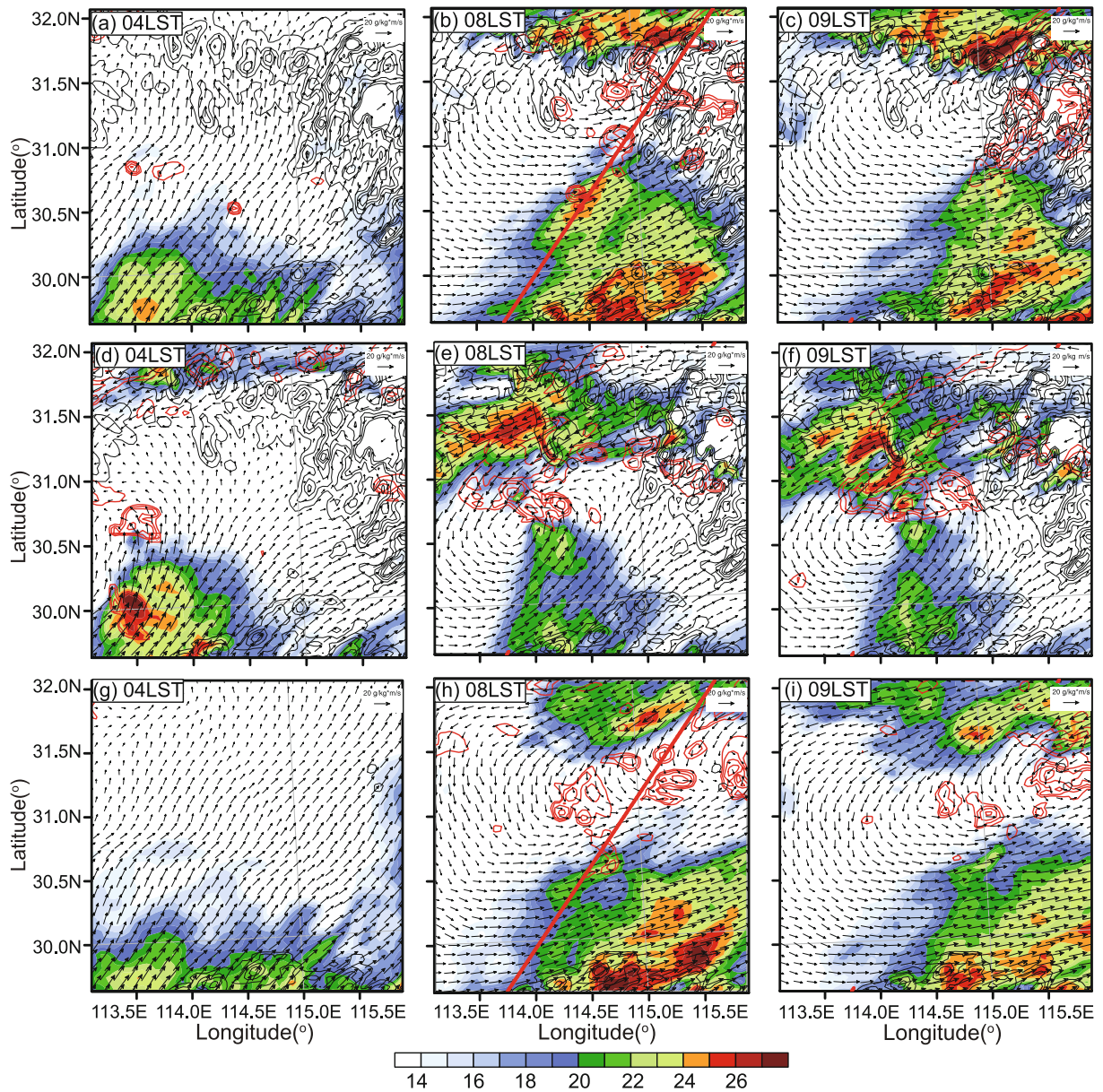
Fig. 13. Water vapor flux (shaded) and wind vector at 950 hPa. The red contours are the forecast composite reflectivity above 35 dBZ: (a) 0400 LST; (b) 0800 LST; (c) 0900 LST. The second and third rows are the same as the first row but for the NoSHF and NoDBM sensitivity experiments, respectively. The red lines indicate the location of the corresponding vertical cross section presented in Fig. 14.

NoDBM experiment is much lower than that of the control experiment (Figs. 14b and e). At 0900 LST, as the perturbation winds turn towards the east, the intensity of water vapor flux for the NoDBM experiment is reduced rapidly (Fig. 14f). Correspondingly, the precipitation is also reduced; while in the control experiment, convection continues to intensify due to orographic lifting by the DBM, although the intensity of water vapor flux is also reduced (Figs. 13c and 14c).

6. Summary

The diurnal cycle of mei-yu precipitation in the year 2013 over the DBM is studied using a dense network of surface

rain gauges and WRF forecasts at 4-km horizontal grid spacing. The spatial rainfall distributions based on the observations reveal a rainfall center over the DBM and its upwind side relative to the background synoptic southwesterly flow. As many previous studies in the YHRB region suggest, the precipitation diurnal cycle over the DBM exhibit a bimodal pattern, with a morning peak at 0800 LST and a secondary afternoon peak at 1300 LST. The 4-km NJU_WRF forecasts successfully reproduce the spatial patterns of rainfall in the YHRB, and capture the rainfall center over the DBM. The temporal variations of rainfall, especially the bimodal pattern, are well forecast, with good agreement with observations in terms of magnitude, although the timing of peak pre-
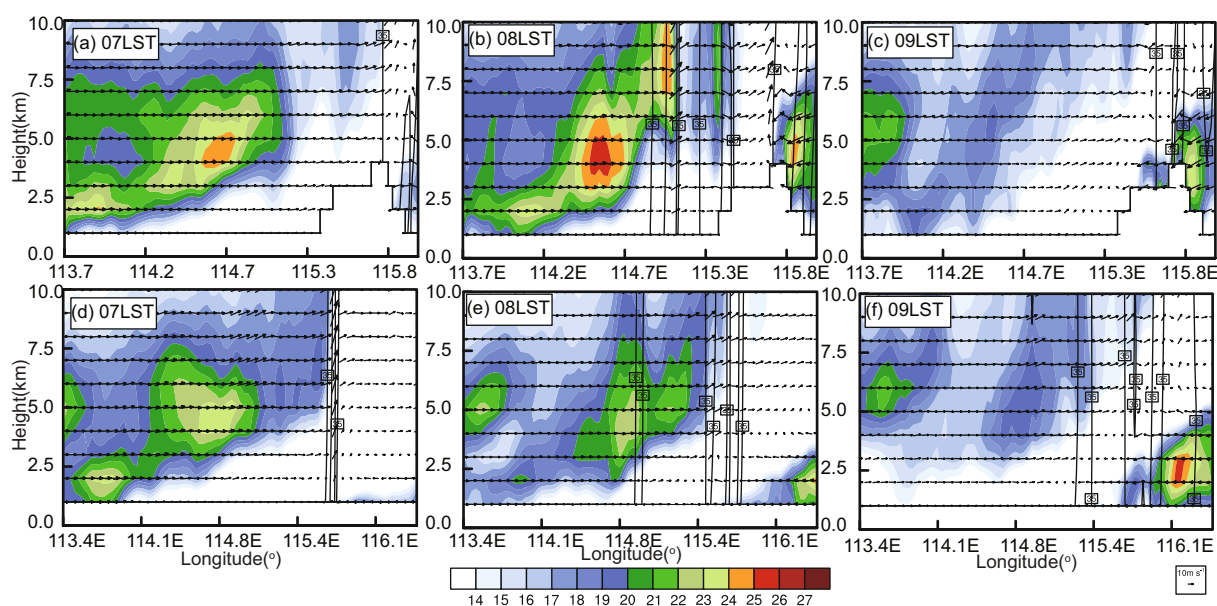
Fig. 14. Vertical slice of water vapor flux (shaded) and wind vector through the red line in Fig. 13. The black contours are the forecast reflectivity above 35 dBZ: (a–c) forecast from the control experiment at 0700 LST, 0800 LST and 0900 LST, respectively; (d–f) as in (a–c) but from experiment NoDBM.

cipitation is slightly delayed by about an hour. The correlation coefficient of hourly mean precipitation between the NJU_WRF forecasts and observations is as high as 0.83. The NJU_WRF forecast winds are also validated against twice-daily radiosonde observations. The forecast wind profiles compare well with observations. The elevation of the low-level (below 900 hPa) peak winds is lower in the forecasts than in the observations, although this might be attributable to the coarse vertical resolution of the sounding data.

Validated against observations, the NJU_WRF forecasts are then used to investigate the formation mechanism of the morning precipitation peak over the DBM. After sunset at 2000 LST, precipitation begins to form in the southwest of the DBM and then propagates towards the foot of the mountains. There is a strong breakout of rainfall along the windward side of the mountains from 0500 to 0800 LST, which results in the morning precipitation peak over the DBM. This local intensification is found to be related to the BLJ and the local topography. Diurnal oscillation results in a clockwise turning of the boundary layer winds, leading to a nocturnal low-level wind maximum in the overnight hours. When the direction of perturbation winds is aligned with the prevailing synoptic-scale southwesterly at 0500 LST, the boundary layer winds reach maximum intensity. This helps transport the moisture-rich southwesterly air along the foothills to the top of the DBM. As the BLJ impinges upon the mountains, it is forced into a convective updraft, resulting in the formation of subsequent precipitation around the DBM a few hours later.

In order to identify the impact of the BLJ and the mountain topography on morning precipitation, two additional experiments are conducted. One involves setting the surface heat flux to zero to examine the impact of the BLJ, and the

other removing the DBM in the model terrain. A typical mei-yu front case is selected to conduct sensitivity experiments. In the control experiment, the precipitation intensifies as the BLJ intensifies. When convection moves up towards the DBM, the precipitation further intensifies. In the experiment without heat flux, without acceleration of wind during the night, the strength of the BLJ in the early morning is significantly reduced. However, in this case, convection continues to grow as the mei-yu front moves to the south. That does not mean the intensification of the BLJ makes no contribution. The intensification of convection is likely contributed by both the intensification of the BLJ and the increased strength of the mei-yu outflow as the mei-yu front heads towards the south. In the other experiment, where the mountain topography is removed, precipitation intensification over the DBM between 0800 and 0900 LST is no longer found. The orographic lifting of the DBM is believed to be the main factor behind precipitation intensification during that time period.

REFERENCES

Bao, X. H., F. Q. Zhang, and J. H. Sun, 2011: Diurnal variations of warm-season precipitation East of the Tibetan Plateau over China. *Mon. Wea. Rev.*, **139**, 2790–2810, https://doi.org/10.1175/MWR-D-11-00006.1.

Blackadar, A. K., 1957: Boundary layer wind maxima and their significance for the growth of nocturnal inversions. *Bull. Amer. Meteor. Soc.*, **38**, 283–290.

Chen, G. X., W. M. Sha, and T. Iwasaki, 2009: Diurnal variation of precipitation over southeastern China: Spatial distribution and its seasonality. *J. Geophys. Res.*, **114**, D13103, https://doi.org/10.1029/2008JD011103.

Chen, H. M., R. C. Yu, J. Li, W. H. Yuan, and T. J. Zhou, 2010: Why nocturnal long-duration rainfall presents an eastward-delayed diurnal phase of rainfall down the Yangtze River Valley. *J. Climate*, **23**, 905–917, https://doi.org/10.1175/2009JCLI3187.1.

Chen, Y.-L., X. A. Chen, and Y.-X. Zhang, 1994: A diagnostic study of the low-level jet during TAMEX IOP 5. *Mon. Wea. Rev.*, **122**, 2257–2284, https://doi.org/10.1175/1520-0493(1994)122<2257:ADSOTL>2.0.CO;2.

Chen, Y.-L., and J. Li, 1995: Large-scale conditions favorable for the development of heavy rainfall during TAMEX IOP 3. *Mon. Wea. Rev.*, **123**, 2978–3002, https://doi.org/10.1175/1520-0493(1995)123<2978:LSCFFT>2.0.CO;2.

Chen, Y.-L., X. A. Chen, S. Chen, and Y.-H. Kuo, 1997: A numerical study of the low-level Jet during TAMEX IOP 5. *Mon. Wea. Rev.*, **125**, 2583–2604, https://doi.org/10.1175/1520-0493(1997)125<2583:ANSOTL>2.0.CO;2.

Collins, W. D., P. J. Rasch, B. A. Boville, J. J. Hack, J. R. Mc-Caa, D. L. Williamson, J. T. Kiehl, and B. Briegleb, 2004: Description of the NCAR Community Atmosphere Model (CAM 3.0). NCAR Technical Note NCAR/TN-464+STR.

Dai, A. G., F. Giorgi, and K. E. Trenberth, 1999: Observed and model-simulated diurnal cycles of precipitation over the contiguous United States. *J. Geophys. Res.*, **104**, 6377–6402, https://doi.org/10.1029/98JD02720.

Ding, Y. H., 1992: Summer monsoon rainfalls in China. *J. Meteor. Soc. Japan*, **70**, 373–396, https://doi.org/10.2151/jmsj1965.70.1B_373.

Ding, Y. H., and J. C. L. Chan, 2005: The East Asian summer monsoon: An overview. *Meteor. Atmos. Phys.*, **89**, 117–142, https://doi.org/10.1007/s00703-005-0125-z.

Du, Y., Q. H. Zhang, Y. Ying, and Y. M. Yang, 2012: Characteristics of low-level jets in Shanghai during the 2008–2009 warm seasons as inferred from wind profiler radar data. *J. Meteor. Soc. Japan*, **90**, 891–903, https://doi.org/10.2151/jmsj.2012-603.

Du, Y., Q. H. Zhang, Y. L. Chen, Y. Y. Zhao, and X. Wang, 2014: Numerical simulations of spatial distributions and diurnal variations of low-level jets in China during Early summer. *J. Climate*, **27**, 5747–5767, https://doi.org/10.1175/JCLI-D-13-00571.1.

Du, Y., R. Rotunno, and Q. H. Zhang, 2015: Analysis of WRF-simulated diurnal boundary layer winds in eastern China using a simple 1D model. *J. Atmos. Sci.*, **72**, 714–727, https://doi.org/10.1175/JAS-D-14-0186.1.

Geng, B., H. Yamada, K. K. Reddy, H. Uyeda, and Y. Fujiyoshi, 2009: Mesoscale development and along-frontal variation of a Meiyu/Baiu front and precipitation observed in the downstream region of the Yangtze River. *J. Meteor. Soc. Japan*, **87**, 423–457, https://doi.org/10.2151/jmsj.87.423.

He, Z. W., Q. H. Zhang, and J. Sun, 2016: The contribution of mesoscale convective systems to intense hourly precipitation events during the warm seasons over central East China. *Adv. Atmos. Sci.*, **33**, 1233–1239, https://doi.org/10.1007/s00376-016-6034-x.

He, Z. W., Q. H. Zhang, L. Q. Bai, and Z. Y. Meng, 2017: Characteristics of mesoscale convective systems in central East China and their reliance on atmospheric circulation patterns. *International Journal of Climatology*, **37**, 3276–3290, https://doi.org/10.1002/joc.4917.

Li, J., Y.-L. Chen, and W.-C. Lee, 1997: Analysis of a heavy rainfall event during TAMEX. *Mon. Wea. Rev.*, **125**, 1060–1082, https://doi.org/10.1175/1520-0493(1997)125<1060:AOAHRE>2.0.CO;2.

Luo, Y. L., W. M. Qian, R. H. Zhang, and D.-L. Zhang, 2013a: Gridded hourly precipitation analysis from high-density rain gauge network over the Yangtze–Huai Rivers Basin during the 2007 Mei-Yu season and comparison with CMORPH. *Journal of Hydrometeorology*, **14**, 1243–1258, https://doi.org/10.1175/JHM-D-12-0133.1.

Luo, Y. L., H. Wang, R. H. Zhang, W. M. Qian, and Z. Z. Luo, 2013b: Comparison of rainfall characteristics and convective properties of monsoon precipitation systems over South China and the Yangtze and Huai River Basin. *J. Climate*, **26**, 110–132, https://doi.org/10.1175/JCLI-D-12-00100.1.

Mass, C. F., D. Ovens, K. Westrick, and B. A. Colle, 2002: Does increasing horizontal resolution produce more skillful forecasts?: The results of two years of real-time numerical weather prediction over the Pacific Northwest. *Bull. Amer. Meteor. Soc.*, **83**, 407–430, https://doi.org/10.1175/1520-0477(2002)083<0407:DIHRPM>2.3.CO;2.

Morrison, H., J. A. Curry, and V. I. Khvorostyanov, 2005: A new double-moment microphysics parameterization for application in cloud and climate models. Part I: Description. *J. Atmos. Sci.*, **62**, 1665–1677, https://doi.org/10.1175/JAS3446.1.

Nesbitt, S. W., and E. J. Zipser, 2003: The diurnal cycle of rainfall and convective intensity according to three years of TRMM measurements. *J. Climate*, **16**, 1456–1475, https://doi.org/10.1175/1520-0442-16.10.1456.

Pleim, J. E., 2006: A simple, efficient solution of flux profile relationships in the atmospheric surface layer. *Journal of Applied Meteorology and Climatology*, **45**, 341–347, https://doi.org/10.1175/JAM2339.1.

Pleim, J. E., 2007: A combined local and nonlocal closure model for the atmospheric boundary layer. Part I: Model description and testing. *Journal of Applied Meteorology and Climatology*, **46**, 1383–1395, https://doi.org/10.1175/JAM2539.1.

Skamarock, W. C., and Coauthors, 2005: A Description of the Advanced Research WRF Version 2. NCAR Technical Note NCAR/TN-475+STR.

Sun, J. H., and F. Q. Zhang, 2012: Impacts of mountain–plains solenoid on diurnal variations of rainfalls along the Mei-Yu front over the East China plains. *Mon. Wea. Rev.*, **140**, 379–397, https://doi.org/10.1175/MWR-D-11-00041.1.

Van De Wiel, B. J. H., A. F. Moene, G. J. Steeneveld, P. Baas, F. C. Bosveld, and A. A. M. Holtslag, 2010: A conceptual view on inertial oscillations and nocturnal low-level jets. *J. Atmos. Sci.*, **67**, 2679–2689, https://doi.org/10.1175/2010JAS3289.1.

Wallace, J. M., 1975: Diurnal variations in precipitation and thunderstorm frequency over the conterminous United States. *Mon. Wea. Rev.*, **103**, 406–419, https://doi.org/10.1175/1520-0493(1975)103<0406:DVIPAT>2.0.CO;2.

Wang, C.-C., G. T.-J. Chen, and R. E. Carbone, 2005: Variability of warm-season cloud episodes over East Asia based on GMS infrared brightness temperature observations. *Mon. Wea. Rev*, **133**, 1478–1500, https://doi.org/10.1175/MWR2928.1.

Weisman, M. L., W. C. Skamarock, and J. B. Klemp, 1997: The resolution dependence of explicitly modeled convective systems. *Mon. Wea. Rev.*, **125**, 527–548, https://doi.org/10.1175/1520-0493(1997)125<0527:TRDOEM>2.0.CO;2.

Xu, W. X., and E. J. Zipser, 2011: Diurnal variations of precipitation, deep convection, and lightning over and East of the Eastern Tibetan Plateau. *J. Climate*, **24**, 448–465, https://doi.org/10.1175/2010JCLI3719.1.

Yamada, H., B. Geng, H. Uyeda, and K. Tsuboki, 2007: Thermodynamic impact of the heated landmass on the nocturnal evolution of a cloud cluster over a Meiyu-Baiu front. *J. Meteor. Soc. Japan*, **85**, 663–685, https://doi.org/10.2151/jmsj.85.663.

Yu, R. C., T. J. Zhou, A. Y. Xiong, Y. J. Zhu, and J. M. Li, 2007: Diurnal variations of summer precipitation over contiguous China. *Geophys. Res. Lett.*, **34**, L01704, https://doi.org/10.1029/2006GL028129.

Yuan, W. H., R. C. Yu, H. M. Chen, J. Li, and M. H. Zhang, 2010: Subseasonal characteristics of diurnal variation in summer monsoon rainfall over central eastern China. *J. Climate*, **23**, 6684–6695, https://doi.org/10.1175/2010JCLI3805.1.

Yuan, W. H., R. C. Yu, M. H. Zhang, W. Y. Lin, H. M. Chen, and J. Li, 2012: Regimes of diurnal variation of summer rainfall over subtropical East Asia. *J. Climate*, **25**, 3307–3320, https://doi.org/10.1175/JCLI-D-11-00288.1.

Yuan, W. H., R. C. Yu, M. H. Zhang, W. Y. Lin, J. Li, and Y. F. Fu, 2013: Diurnal cycle of summer precipitation over subtropical East Asia in CAM5. *J. Climate*, **26**, 3159–3172, https://doi.org/10.1175/JCLI-D-12-00119.1.

Zheng, Y. G., M. Xue, B. Li, J. Chen, and Z. Y. Tao, 2016: Spatial characteristics of extreme rainfall over China with hourly through 24-hour accumulation periods based on national-level hourly rain gauge data. *Adv. Atmos. Sci.*, **33**, 1218–1232, https://doi.org/10.1007/s00376-016-6128-5.

Zhu, K. F., and M. Xue, 2016: Evaluation of WRF-based convection-permitting multi-physics ensemble forecasts over China for an extreme rainfall event on 21 July 2012 in Beijing. *Adv. Atmos. Sci.*, **33**, 1240–1258, https://doi.org/10.1007/s00376-016-6202-z.

Zhu, K. F., and Coauthors, 2018: Evaluation of real-time convection-permitting precipitation forecasts in China during the 2013–2014 summer season. *J. Geophys. Res.*, **123**, 1037–1064, https://doi.org/10.1002/2017JD027445.